Metal pad instability in Liquid Metal Batteries

by

Linyan Xiang

A thesis submitted in partial fulfillment
of the requirements for the degree of
Master of Science in Engineering
(Mechanical Engineering)
in the University of Michigan-Dearborn
2018

Master's Thesis Committee:

Professor Oleg Zikanov, Chair
Professor Ben Q. Li
Professor Subrata Sengupta

To my parents

ACKNOWLEDGEMENTS

I wish to express my deepest gratitude to my supervisor, Professor Oleg Zikanov, for his continuous support, guidance and constructive criticism on not only my research but also my understanding of the life.

I also own many thanks to Dr. Norbert Weber for all the helpful advices and discussions during the research.

I wish to thank all the members and predecessors of the Computational Fluid Dynamics Lab with whom I had numerous fruitful discussions.

My thanks also go to my family and friends for their support and encouragement throughout the research.

Wish that my best time was spent with them, and with me forever.

TABLE OF CONTENTS

LIST OF FIGURES

ABSTRACT

The Liquid Metal Battery (LMB) is a new promising concept of a device for large-scale stationary energy storage. The ongoing development and commercialization of the LMB faces the problem of disruptions of operation caused by the magneto-hydrodynamic instabilities. One of the instabilities, the metal pad instability, is modeled and analyzed in the thesis work. The numerical model is based on the open-source CFD software OpenFOAM, modified to include electromagnetic effects and address the numerical aspects related to strong variations of fluid parameters. The model is applied to investigate the effects of the thickness of electrolyte, strength of magnetic field, and the metal and electrolyte densities on the instability. One conclusion of the study is that the metal pad instability can be simulated using properly modified general-purpose CFD software. Another conclusion is that the instability is the potentially serious problem that has to be addressed in the LMB design.

CHAPTER I

Introduction

1.1 Liquid metal battery as a possible solution for grid storage problem

The development of the renewable energy requires development of energy storage methods. The reason is the intermittency of the sustainable energy sources. The storage methods have to be low-cost, long-lasting and satisfy the requirements of scalability to large sizes and high charging discharging rate. Existent solutions, such as Li-ion batteries, pumped hydro storage and compressed air, are widely implemented and commercialized to grid storage (4). However, these grid storage solutions are not perfect. For example, Li-ion batteries are subjected to material degradation, which can seriously limit their lifecycle ((9), (7)). The pumped hydro storage is limited by availability of suitable geographic locations. Thus, a new large-scale storage solution with easy-to-get materials and long life-cycle is required in short-term perspective.

The physical principle was first proposed in 1958, in the form of a thermally regenerative battery (9). Intense research on development of the device, also called the Liquid Metal Battery(LMB) was conducted at the GM's research department and Argonne National Lab (9). However, the development was slowed down for the following few decades because of the low specific energy density, which made battery unusable for mobile applications (9). After enduring several decades of stagnation, the development of liquid metal battery was

reactivated by Professor Sadoway's team from MIT in 2012. The aims was to develop a low-cost, enduring energy storage device.

In general, the batteries work as the oxidation reactions occurs at the electrodes and convert the electrochemical energy into electrical energy. The chemical potential difference between anode and cathode specify the cell's open circuit voltage. The principle of LMBs' operation is different from Li-ion batteries. A typical Li-ion battery consists of anode, cathode, separator, and electrolyte. During the charging process, lithium in positive electrode is ionized and inserted into the negative layer through electrolyte. During the discharging processes, lithium ions are dissociated from the anode and inserted into the crystal structure of the cathode(e.g., specialty carbon) through the electrolyte. But the principle of Liquid Metal Batteries' operation is different as illustrated in Figure.1.1.

It contains three liquid layers. The lighter metal is located at the top. The heavier metal stays at the bottom. The electrolyte is sandwiched in the middle. Because of the density difference and the immiscibility of the metals with the electrolyte, the battery system can be stable with the natural self-segregation of all-liquid components.

While the liquid metal battery is discharging, the oxidation reaction occurs at the top in the alkali/earth-alkali (e.g., Li, Na, Mg) metal A. Electrons flow from the anode(top metal layer) to the cathode. Ions of metal A pass through the molten salt electrolyte and reduce to atoms A after receiving the electrons within the bottom layer. The reaction at the anode/electrolyte and electrolyte/cathode interface during the discharge can be formulated as follows:

$$\begin{aligned} A &\rightarrow A^{z+} + ze^{-} \\ A^{z+} + ze^{-} &\rightarrow A\,(N)\,, \end{aligned} \tag{1.1}$$

with A denoting the alkali or the earth-alkali metal (e.g., Na, Li, Ca, Mg), N representing the heavy metal at the bottom layer(e.g., Bi, Sb, Zn, or PbSb) (28). The z denotes the valence, i.e., 1 for alkali and 2 for earth alkali metals (25). The reactions and flows of the electrons and ions are reversed when the battery is charging.

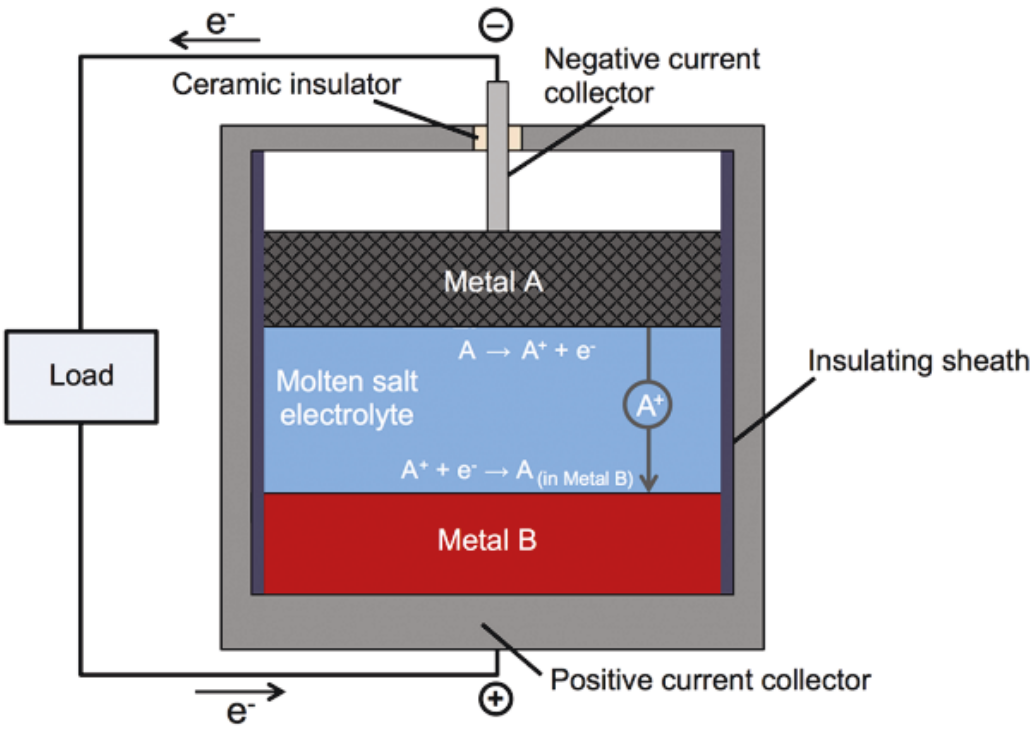

Figure 1.1: Principal design of a Liquid Metal Battery in the discharging mode. Ref: http://news.mit.edu/2016/battery-molten-metals-0112

One important property of the LMBs is their potentially very low cost. As agreed, for example, in (9), the cheap manufacturing materials make it theoretically possible to build a battery with cost below $100 per KWh of capacity. To achieve this goal, large batteries (size 1m) must become technologically possible.

The liquid metal batteries' all-liquid nature has drawn the attention of fluid scientists to investigate the fluid mechanics. There are several topics under the fluid mechanics of Liquid Metal Batteries: Tayler instability (23), thermal convection instability (18), Marangoni instability (11) and the metal pad instability. The existance of metal pad instability in LMB was first suggested in (27) where the analogy with the instability mechanism of aluminum reduction cell was used. Although the model was based on reducing the top and bottom electrodes into slabs of solid metal instead of liquid that have infinite degrees of freedom, it well illustrated the physical mechanism of the metal pad instability. Then the metal pad instability mechanism was further validated in (22), where instability properties mechanism

of a cylindrical battery were studied numerically.

In conventional batteries, the microstructural degradation of solid electrodes is the most important factor for the limiting life of battery. In contrast, the liquid metal battery is competitive because the electrodes are liquid and, thus, inherently immune to the microstructural degradation (9). Therefore, the lifetime of battery can be profoundly extended.

The liquid state of the electrodes also presents a disadvantage. The fluid dynamics effects can seriously impacts the stability of the metal electrolyte interfaces, which may cause a short circuit between the electrodes, thus disrupting the operation.

1.2 Metal pad instability

This thesis addresses one of the possible mechanism leading to such behavior, namely the metal pad instability. It is the phenomenon influenced by the magnetic field induced by neighboring cells and supply lines. A similar instability was found in the aluminum reduction cells ((3), (17), (19)). While the batteries are in charging or discharging, the liquid metals are driven by the Lorentz force due to the interaction of the operating electric current and magnetic field. Under specific parameters of the system, this leads to instability generating growing waves at the interface between electrolyte and electrodes. In the worst case, the metals at the top and bottom come to contact with each other to give rise to the short circuit. In this case, the stability of the liquid metal battery can be seriously affected. Hence, the mechanism of the instability needs to be investigated in order to optimize the LMBs design. In the hydrodynamic perspective, the metal pad instability is defined as a electrical-magnetically enhanced waves on interface between liquid metal and molten salt electrolyte grown from the weak initial perturbations. In the operation of LMBs perspective, the metal pad instability is defined as the short circuit of the LMBs from the growth of wave.

In the thesis work, the battery is modeled as a cuboid with three immiscible liquid layers. The mechanism of the instability can be briefly described as follows. When the

liquid metal battery is in operation, even a tiny perturbation leads to non-uniformity of the electrolyte thickness. The non-uniform geometry of the electrolyte further leads to the perturbation of electric currents flowing within the battery. The perturbation of the electric currents gives rise to the electric potential difference in the horizontal plane. Therefore, the local electric currents in the horizontal direction are generated in the metal layers. If an extenally generated magnetic field is presented, this leads to the Lorentz force that may work as a destabilizing force on the whole system. The instability occures as growing sloshing waves at the interfaces. The metal pad instability mechanism is further detailed and illustrated in following sections.

The metal pad instabilitiy was studied for the Hall-Héroult aluminum reduction cells which can be seen as systems similar to that in Figure 1.1, but shallow and without the top metal layer (see, e.g. (3)). For the LMB, the possibility of the instability was first considered in (27) using a mechanical analogy. The relation between the magnetic field, electric current and motion of pendulums imitating the metla layers was described. Then, a numerical model was developed to simulate the instability in cylindrical liquid metal batteries (22). The non-dimensional parameters were introduced to describe the instability in (28) and (22). The non-dimensional parameter introduced in (28) is used in the present study.

CHAPTER II

Physical and Mathematical Model

The Liquid Metal Battery is a complex electro-hydromagnetic system even if it is considered in the framework of a simplified model. The system's operation includes various mechanisms, some of which are unknown. Therefore, a reasonable first step is to investigate each mechanism individually, isolated from the rest. For example, the Tayler instability is investigated ignoring the layered nature of the system and heating in (16), (20), (24). The thermal convection is explored ignoring the effects of the deformation of the interface (18).

This thesis will analysize the isolated effect of the metal pad instability. The effects of the Tayler instability, thermal convection instability, Marangoni instability and electrovortex flow are ignored.

2.1 The simplifying assumptions

2.1.1 Simplified model of magnetic field

The typical magnetic field of a Liquid Metal Battery is three-dimensional and possibly unsteady. Part of the field is induced by the currents flowing through the battery. It is primarily horizontal. The other part is truly three-dimensional and is generated by the currents flowing in supply lines and neighboring battery cells (17). By the analogy with the instability in aluminum reduction cells ((3), (17), (19)) that the metal pad instability

is caused by the vertical component of the magnetic field. For this reason, we neglect all components but the vertical one, which is approximated by a constant.

2.1.2 The liquid metal battery is operated under proper care to avoid the solid intermetallic form of the metal

The intermetallic solid formation is viewed as one of the serious causes for the failure of liquid metal battery (8). During the discharge stage of LMBs, poor mixing is likely to cause the formation of intermetallic solid below the interface between the bottom electrode and electrolyte. It would change the flow pattern due to the low thermal and electrical conductivity of the solid (8).

2.1.3 Incompressible, Newtonian, electrically conducting fluid

Each fluid is assumed to be incompressible, Newtonian and having a constant electrical conductivity. The properties are, however, different among the two molten metals and the electrolyte.

2.1.4 Surface tension is insignificant

The coupling between the flows in the three layers via viscous shear force, pressure force and Lorentz force is introduced in the model. The thermocapillary Marangoni effect, the most well-studied surface tension effect in the LMB ((8), (11)) is absent in our mode due to the assumption of constant temperature (see section 2.1.6). The surface tension itself is included. We note, however, that the curvature of the interfaces remains small even is strongly unstable cases. The surface tension forces, therefore, are insignificant.

2.1.5 Quasi-static approximation of electromagnetic effects

If the external magnetic field **B** is explicitly separated from the induced magnetic field **b**, the quasi-static approximation can be applied in the MHD equations at low magnetic

Reynolds numbers. It is known that the quasi-static approximation is valid at the magnetic Reynolds numbers $\mathrm{Re}_m < 0.1$ ((3), (10)). In the approximation, the induced magnetic field is neglected in comparison with the imposed field in the expressions for the Ohm's law and Lorentz force. The approximation can be derived theoretically ((3), (10)) and has been thoroughly validated in comparison with experiments.

In our case, $\mathrm{Re}_m = UL\cdot\sigma\mu_o$ can be estimated by taking $L = 0.1m, U \approx 10^{-3}\ or\ 10^{-2}\ m/s$, $\sigma = 80$ or $3.62\times10^6\ S/m$, $\mu_o = 4\pi\times10^{-7}\ Pa\cdot s$ which gives

$$\begin{aligned}[\mathrm{Re}_m]_{\max} &= UL\cdot\sigma\mu_o = 10^{-2}\times0.1\times3.62\times10^6\times4\pi\times10^{-7}\\ &= 4.549\times10^{-3} < 0.1.\end{aligned} \tag{2.1}$$

Thus, the quasi-static approximation is valid.

2.1.6 Constant temperature

The liquid metals inside the model are assumed to be maintained at a constant temperature so that the effects of thermal and Marangoni convection will not affect the results. The approximation is justified by the results of (18), (9) and (11) which show that the thermal and Marangoni convection inevitably present in the battery are unlikely to perturb the interfaces strongly under typical operational conditions.

2.1.7 Immiscible fluids

The liquid metals forming the top and bottom layers of the liquid metal battery are assumed to be immiscible with the electrolyte forming the middle layer.

2.2 Governing equations

The governing equations of the model are introduced in this section. The main difference compared with the conventional fluid equations is that we add the Lorentz body force

and utilize the makrer equation to determine the location of the interface. The governing equations include:

Continuity equation

$$\nabla \cdot \mathbf{U} = 0, \tag{2.2}$$

where $\mathbf{U} = \alpha_{top}\mathbf{U}_{top} + \alpha_{electrolyte}\mathbf{U}_{electrolyte} + \alpha_{bottom}\mathbf{U}_{bottom}$.

Momentum equation (15)

$$\frac{\partial \rho \mathbf{U}}{\partial t} + \nabla \cdot (\rho \mathbf{U}\mathbf{U}) = -\nabla p + \nabla \cdot \left[\mu(\nabla \mathbf{U} + \nabla \mathbf{U}^T)\right] + \rho\,(\mathbf{f}_L + \mathbf{g}) + \mathbf{f}_{st}, \tag{2.3}$$

where t, $\mathbf{U}$, ρ, p, μ, $\mathbf{f}_L$, $\mathbf{g}$ and $\mathbf{f}_{st}$ represent the time, velocity field, density, pressure, dynamic viscosity, Lorentz body force, acceleration of gravity and the surface tension force.

The Lorentz force $\mathbf{f}_L$ is the result of the interaction between the electric current $\mathbf{J}$ and the magnetic field $\mathbf{B}$:

$$\mathbf{f}_L = \mathbf{J} \times \mathbf{B}, \tag{2.4}$$

where electric current density $\mathbf{J}$ is calculated by the Ohm's law. The Ohm's law reads:

$$\mathbf{J} = \sigma(-\nabla \phi + \mathbf{U} \times \mathbf{B}), \tag{2.5}$$

where σ is the electric conductivity of the fluid.

Following the quasi-static approximation, only the steady-state imposed component of the magnetic field is represented by $\mathbf{B}$. The additional field $\mathbf{b}$ included by the current perturbations is assumed to be negligible in comparison with $\mathbf{B}$.

Demanding the charge conservation $\nabla \cdot \mathbf{J} = 0$, we obtain the elliptic equation for the electric potential:

$$\nabla \cdot (\sigma \nabla \phi) = \nabla \cdot (\sigma (\mathbf{U} \times \mathbf{B})). \tag{2.6}$$

Three immiscible layers in the multiphase flow are identified by the marker equation:

$$\frac{D\alpha_i}{Dt} = \frac{\partial \alpha_i}{\partial t} + \nabla \cdot (\alpha_i \mathbf{U}) = 0, \tag{2.7}$$

in which α_i represents the fraction of a phase, i.e., α_{top} is the fraction of positive electrode metal, $\alpha_{electrolyte}$ is the fraction of electrolyte, and α_{bottom} is the fraction of negative electrode metal at a given location.

The sum of the three layers' markers is 1.

$$\alpha_{top} + \alpha_{electrolyte} + \alpha_{bottom} = 1 \tag{2.8}$$

where α_i takes the value from 0 to 1. The value of 1 represents the region that only have one single phase. For example, $\alpha_{top} = 1$ represents the location within the top metal layer, $\alpha_{electrolyte} = \alpha_{bottom} = 0$ in this layer. In the areas around the interfaces, intermediate values of α_i can be found. This is the effect of the numerical diffusion, and is tolerated in the model, provided the thickness of the diffused interface remains small (1). The interface between different fluids can be tracked using the value of α_i. In the computational model, the three immiscible fluids are considered as one effective fluid throughout the domain. The physical properties stored at the center of cells are calculated from the weighted fractions of three different phases. For example, the dynamic viscosity is computed as $\mu = \mu_{top}\alpha_{top} + \mu_{electrolyte}\alpha_{electrolyte} + \mu_{bottom}\alpha_{bottom}$.

According to the Faraday's law, the non-uniform electrolyte thickness results in the local current perturbations $\mathbf{j}$ (see Figure 2.1). The Lorentz body force is generated by the interaction between the horizontal component of the induced local electric current $\mathbf{j}$ and the vertical component of the magnetic field. Such a Lorentz body force has a destabilizing effect in the flow (Figure 2.1).

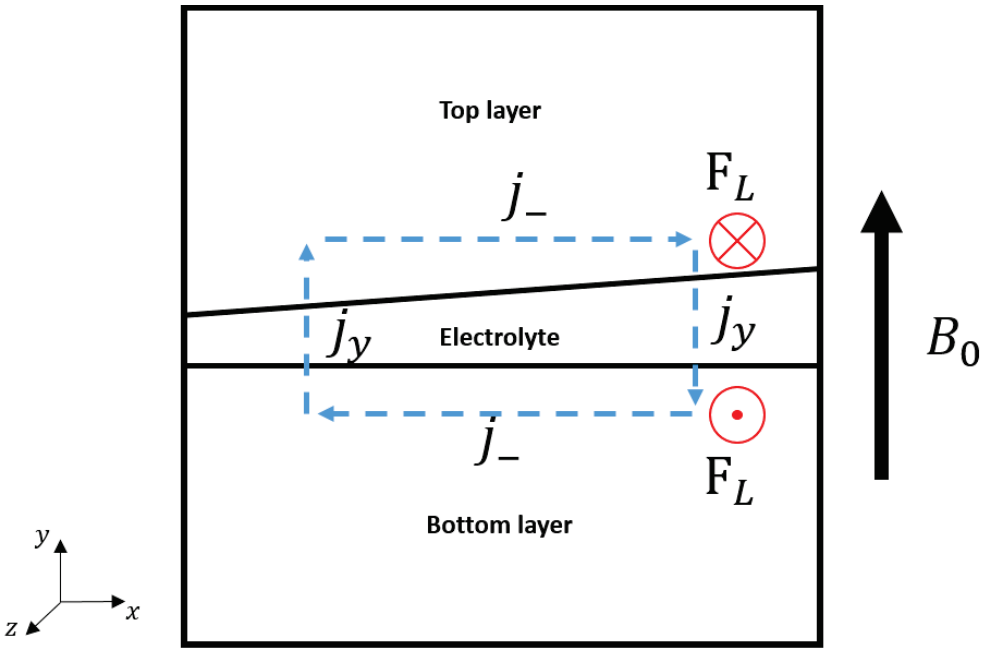

Figure 2.1: Schematic representation of the physical mechanism of the metal pad instability. The local electric current is induced by the horizontal electric potential difference due to the non-uniform thickness of the electrolyte. It is further discussed later in the text.

Dimensionless equations are not used in our work because the three different layers have different properties, e.g. viscosity, density and electric conductivity, which result in a large number of dimensionless parameters. For example, the Reynolds number, which is calculated by the fluid properties of density and viscosity, has three different values in the three layers. Therefore, the dimensional governing equations are used during the simulation.

CHAPTER III

Numerical Methods

The evolution of a three-dimensional unsteady flow is calculated using the Finite Volume Method described in (13) and extended to flows with multiphase features in ((2), (21)) and flows with the combined effects of sloshing and magnetic field in (22). The details of the method can be found in these references, while the main contribution in the thesis work is to develop the magneto-hydrodynamic feature base on the OpenFOAM's original solver multiphaseInterFoam (6). In the following sections, the discretization schemes of marker equation, momentum equation, continuity equation and electric potential equation are presented. The solving procedure for a time step is presented at the end of this section.

3.1 Discretization approach

3.1.1 Generalization of Gauss integral equations

By implementing the Finite Volume Method (FVM), the discretized equations will be integrated over every node. A single control volume of the structured grid that is used in the simulations can be found in Figure 3.1.

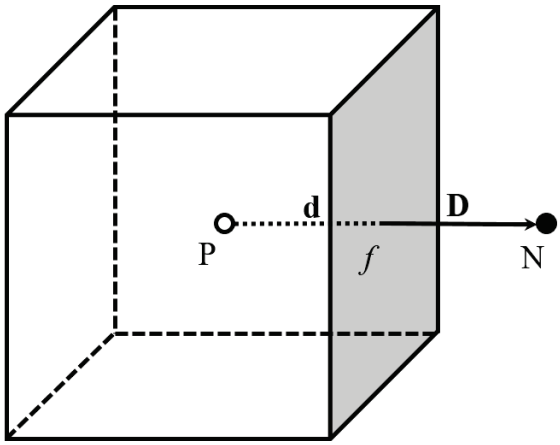

Figure 3.1: Illustration of the single control volume of the structured grid that is used in the simulations. P is the center of the cell, N is the center of neighbouring cell, f is the center of the interface between the owner and the neighbouring cells, **d** is the distance between the center of the cell and the interface, **D** is the distance between the center of the neighbouring cell and the interface

The generalized forms of the Gauss integral and the derivation of the discrete equations are:

$$\int_V \nabla \cdot \boldsymbol{\varphi} dV = \oint_{\partial V} d\mathbf{S} \cdot \boldsymbol{\varphi}, \tag{3.1}$$

$$\int_V \nabla \varphi dV = \oint_{\partial V} d\mathbf{S} \varphi, \tag{3.2}$$

$$\int_V \nabla \times \boldsymbol{\varphi} dV = \oint_{\partial V} d\mathbf{S} \times \boldsymbol{\varphi}, \tag{3.3}$$

where $\boldsymbol{\varphi}$ stands for an arbitrary vector, φ for an arbitrary scalar, d$\mathbf{S}$ for the surface area vector and dV for the control volume.

The control volumes are orthogonal hexahedral with six flat faces. Therefore, the integration over control volume in (3.1)-(3.3) is equivalent to the sum of the integrals over the faces.

For example, equation (3.1) becomes

$$\int_V \nabla \cdot \boldsymbol{\varphi} dV = \oint_{\partial V} d\mathbf{S} \cdot \boldsymbol{\varphi} = \sum_{f=1}^{n} \left(\int_f d\mathbf{S} \cdot \boldsymbol{\varphi} \right) \approx \sum_{f=1}^{n} \mathbf{A}_f \cdot \boldsymbol{\varphi}_f, \tag{3.4}$$

where $\mathbf{A}_f$ is the face area vector and n is the number of faces of a control volume.

The equations (3.1)-(3.3) can also be used to get the second order accurate predictions of the values of differential operators at the centers of the cells:

$$(\nabla \cdot \boldsymbol{\varphi})_P \approx \frac{1}{V_P} \sum_{f=1}^{n} \mathbf{A}_f \cdot \boldsymbol{\varphi}_f, \tag{3.5}$$

$$(\nabla \varphi)_P \approx \frac{1}{V_P} \sum_{f=1}^{n} \mathbf{A}_f \varphi_f, \tag{3.6}$$

$$(\nabla \times \boldsymbol{\varphi})_P \approx \frac{1}{V_P} \sum_{f=1}^{n} \mathbf{A}_f \times \boldsymbol{\varphi}_f. \tag{3.7}$$

The discretization equations above are used in the derivation of the governing equations in the following sections.

3.1.2 Face addressing technique in the spatial discretization

A face addressing technique is used for the finite volume method. The objective of this technique is to arrange the discretized nodes into an organized number array. Thus, it will be able to improve the computational efficiency and conveniency of recognizing the owner and neighbor faces. This arrangement simplifies the computer programming and minimized the geometry information required for the computational grid (21). The approach in (6) is meant for solutions on non-orthogonal grids. In our case, the orthogonal grid is used. However, the face addressing technique is still an ideal way to organize the grid for its convenience at recognition of face owner and neighbor.

The faces of the cells are numbered and categorized into owners and neighbors. Every

face is shared by two neighbouring cells in which one own the face and the other cell is the neighbor. In this way, the face area vector $\mathbf{A}_f$ always points from the owner cell into the neighbour cell of the face. Thus, the summation of the face integrals differs for owner (add into summation) to neighbor as below.

$$\sum_{f=1}^{n} \mathbf{A}_f \cdot \boldsymbol{\varphi}_f = \sum_{\text{owner}} \mathbf{A}_f \cdot \boldsymbol{\varphi}_f - \sum_{\text{neighbour}} \mathbf{A}_f \cdot \boldsymbol{\varphi}_f \tag{3.8}$$

3.2 Marker equation

Before introducing the marker equation, it is necessary to introduce the marker function α. The Volume of Fluid (VOF) method, one of the most well-established versions of the marker-and-cell method (MAC), is used here (1). The marker α is defined as the volume of the fluid A in a control volume over the entire volume.

$$\alpha_{phase} = \frac{\text{volume of fluidA}}{\text{volume of the control volume}} \tag{3.9}$$

For incompressible fluids, the governing equation describing the conservation of phase in the integral form is:

$$\int_{t}^{t+\delta t} \left(\int_{V} \frac{\partial \alpha}{\partial t} dV \right) dt + \int_{t}^{t+\delta t} \left(\int_{V} \nabla \cdot \alpha \mathbf{U} dV \right) dt = 0. \tag{3.10}$$

The first term of equation (3.10) can be approximated as:

$$\int_{t}^{t+\delta t} \left(\int_{V} \frac{\partial \alpha}{\partial t} dV \right) dt \approx \int_{t}^{t+\delta t} \left(\frac{\partial \alpha_P}{\partial t} V_P \right) dt \approx \left(\alpha_P^{t+\delta t} - \alpha_P^{t} \right) V_P. \tag{3.11}$$

For the second term of the equation (3.10), the Gauss theorem gives:

$$\begin{aligned}
&\int_t^{t+\delta t}\left(\int_V \nabla\cdot\alpha\mathbf{U}dV\right)dt = \int_t^{t+\delta t}\left(\oint_{\partial V}\alpha d\mathbf{S}\cdot\mathbf{U}\right)dt \\
&\approx \int_t^{t+\delta t}\left(\sum_{f=1}^{n}\alpha_f\mathbf{A}_f\cdot\mathbf{U}_f\right)dt = \int_t^{t+\delta t}\left(\sum_{f=1}^{n}\alpha_f F_f\right),
\end{aligned} \tag{3.12}$$

where volumetric flux F_f at the face is

$$F_f = \mathbf{A}_f\cdot\mathbf{U}_f. \tag{3.13}$$

The time integral of the convection term is discretized by using the Crank-Nicolson schemes (21):

$$\int_t^{t+\delta t}\left(\int_V \nabla\cdot\alpha\mathbf{U}dV\right)dt \approx \int_t^{t+\delta t}\left(\sum_{f=1}^{n}\alpha_f F_f\right)dt = \sum_{f=1}^{n}\frac{1}{2}\left(\alpha_f^t + \alpha_f^{t+\delta t}\right)F_f\delta t. \tag{3.14}$$

Substituting (3.11) and (3.14) into (3.10), we obtain

$$\alpha_P^{t+\delta t}\frac{V_P}{\delta t} + \sum_{f=1}^{n}\frac{1}{2}\alpha_f^{t+\delta t}F_f = S_{\alpha_P}, \tag{3.15}$$

where S_{α_P} is the source term defined as:

$$S_{\alpha_P} = \alpha_P^t\frac{V_P}{\delta t} - \sum_{f=1}^{n}\frac{1}{2}\alpha_f^t F_f. \tag{3.16}$$

Equation (3.15) is the discretized form of the marker equation. Further details can be found in (21).

3.3 Momentum and incompressibility equations

3.3.1 Final form of momentum equation

The momentum equation discretization is present in this section. The continuity equation and the momentum equation are strongly coupled in the problem. Thus, the Pressure Implicit with Splitting of Operators (PISO) algorithm is implemented to decouple these two equations (26).

In the PISO algorithm, the final form of the momentum equation (2.3) can be obtained by reformulating the body force and pressure terms.

The modified pressure is introduced as

$$p^* = p - \rho \mathbf{g} \cdot \mathbf{x}. \tag{3.17}$$

Taking the gradient at both side of equation (3.17),

$$\nabla p^* = \nabla p - \rho \mathbf{g} - \mathbf{g} \cdot \mathbf{x} \nabla \rho. \tag{3.18}$$

The viscous stress term is reformulated as:

$$\nabla \cdot \tau = \nabla \cdot (\mu \nabla \mathbf{U}) + (\nabla \mathbf{U}) \cdot \nabla \mu. \tag{3.19}$$

The surface tension force is reformulated as:

$$\int_{S(t)} \sigma \kappa' \mathbf{n}' \delta \left(\mathbf{x} - \mathbf{x}' \right) dS \approx \sigma \kappa \nabla \alpha, \tag{3.20}$$

where κ is the curvature of the interface given by

$$\kappa = \nabla \cdot \left(\frac{\nabla \alpha}{|\nabla \alpha|} \right). \tag{3.21}$$

Finally, the momentum equation prepared for discretization is:

$$\begin{aligned}&\frac{\partial \rho \mathbf{U}}{\partial t} + \nabla \cdot (\rho \mathbf{U}\mathbf{U}) = \\ &-\nabla p^* + \nabla \cdot (\mu \nabla \mathbf{U}) + (\nabla \mathbf{U}) \cdot \nabla \mu - \mathbf{g} \cdot \mathbf{x} \nabla \rho + \sigma \kappa \nabla \alpha + \rho (\mathbf{f} - \mathbf{g}).\end{aligned} \tag{3.22}$$

3.3.2 Discretization of momentum equation

Following the discretization method introduced in (15), the discretized form of momentum equation is:

$$a_P^U \mathbf{U}_P = \mathbf{H}(\mathbf{U}) - \nabla p_d - \mathbf{g} \cdot \mathbf{x} \nabla \rho + \sigma \kappa \nabla \alpha. \tag{3.23}$$

where the $a_P^U \mathbf{U}_P$ is the diagonal terms of the linear algebraic equations matrix and the $\mathbf{H}(\mathbf{U})$ is the 'H' operator matrix which is the source term of the matrix minors the product of the off-diagonal coefficient matrix and solution matrix (15).

The system of linear algebraic equations reads:

$$\begin{aligned}\mathbf{H}(\mathbf{U}) &= \frac{\rho_P^{n+1}\mathbf{U}_P^{n+1} - \rho_P^n \mathbf{U}_P^n}{\Delta t} V_P + \sum_f \rho_f \phi \mathbf{U}_f^{n+1} \\ &= \sum_f \mu_f \mathbf{S} \cdot \nabla_f \mathbf{U}^{n+1} + (\nabla \mathbf{U}) \cdot \nabla \mu_f.\end{aligned} \tag{3.24}$$

Reformulating it to isolate the velocity at cell centres:

$$\mathbf{U}_P = \left[a_P^U\right]^{-1} \left[\mathbf{H}(\mathbf{U}) - \nabla p_d - \mathbf{g} \cdot \mathbf{x} \nabla \rho + \sigma \kappa \nabla \alpha\right]. \tag{3.25}$$

Then, substituting the velocity as (3.25) in continuity equation. A Poisson equation is generated and is good to be solved in iterative manner.

$$\nabla \cdot \left\{ \left[a_P^U\right]^{-1} \left[\mathbf{H}(\mathbf{U}) - \mathbf{g} \cdot \mathbf{x} \nabla \rho + \sigma \kappa \nabla \alpha\right] \right\} = \nabla \cdot \left\{ \left[a_P^U\right]^{-1} \nabla p_d \right\} \tag{3.26}$$

3.4 Electric potential equation

After solving the marker function and momentum equation, the flow properties are updated. Consequently, the distribution of the electric potential is to be updated. For that, we solve the potential equation

$$\nabla \cdot (\sigma \nabla \phi) = \nabla \cdot (\sigma(\mathbf{U} \times \mathbf{B})). \tag{3.27}$$

Integrating the equation above, we find

$$\int_{\partial V} d\mathbf{S} \cdot (\sigma \nabla \phi) = \int_{\partial V} d\mathbf{S} \cdot (\sigma(\mathbf{U} \times \mathbf{B})). \tag{3.28}$$

Applying the generalized discretization formulas in section 3.1, the equation can be discretized as follow.

Left-hand side of equation (3.28) is discretized as:

$$\begin{aligned} \int_{\partial V} d\mathbf{S} \cdot (\sigma \nabla \phi) &= \sum_{f=1}^{n} \left(\int_{f} d\mathbf{S} \cdot (\sigma \nabla \phi) \right) \\ &\approx \sum_{f=1}^{n} [\sigma_f \mathbf{A}_f \cdot (\nabla \phi)_f]. \end{aligned} \tag{3.29}$$

Right-hand side of equation (3.28) is discretized as:

$$\begin{aligned} \int_{\partial V} d\mathbf{S} \cdot (\sigma(\mathbf{U} \times \mathbf{B})) &= \sum_{f=1}^{n} \left(\int_{f} d\mathbf{S} \cdot (\sigma(\mathbf{U} \times \mathbf{B})) \right) \\ &\approx \sum_{f=1}^{n} [\sigma_f \mathbf{A}_f \cdot (\mathbf{U} \times \mathbf{B})_f]. \end{aligned} \tag{3.30}$$

Finally, the discretized form of the electric potential equation (2.6) is:

$$\sum_{f=1}^{n} [\sigma_f \mathbf{A}_f \cdot (\nabla \phi)_f] = \sum_{f=1}^{n} [\sigma_f \mathbf{A}_f \cdot (\mathbf{U} \times \mathbf{B})_f]. \tag{3.31}$$

3.5 Harmonic interpolation

Since the finite volume method is used, the properties of the field are stored at the centers of the control volumes. After applying the divergence theorem to the conservation equations, the properties at the cell faces are needed to evaluate the surface fluxes. This requires interpolation of the properties from the cell centers to the center points of cell faces. Standard linear interpolation that guarantees the second order accuracy of the entire discretization is used in the model with one important exception. The exception concerns the interpolation of the electrical conductivities and the electrical potential. It is needed because of the large differences of electrical conductivities between the electrolyte and the electrodes (see Table 4.1).

The electrical conductivities σ of the electrodes are about 4 orders of magnitude larger than the conductivity of the electrolyte. It is found that the special interpolation algorithm, which can avoid the numerical error caused by substantial quantity difference between two cells, is an important factor to get accurate results. Therefore, the interpolation of σ in the cells near the electrolyte-electrode interface should be paid special attention. We use the harmonic interpolation, which, as discussed in (14), gives much better accuracy than the standard linear interpolation. To illustrate the effect, two neighbouring cells near the interface are shown in Figure 3.2.

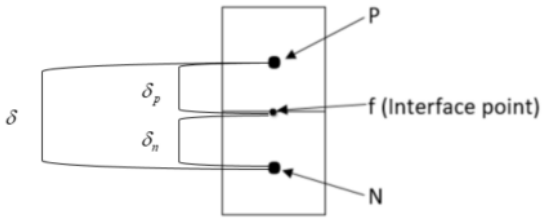

Figure 3.2: Illustration of interpolation over a single cell

The linear interpolation to the face center f is

$$\sigma_f = \frac{\delta_n}{\delta}\sigma_p + \frac{\delta_p}{\delta}\sigma_n. \tag{3.32}$$

For simplicity, we assume that a uniform grid is implemented in the interface area(the grid used in our simulations satisfies this property). For the typical values of metal and electrolyte conductivities (see Table 4.1), we obtain

$$\sigma_f = \frac{1}{2} \times 3.62 \times 10^6 + \frac{1}{2} \times 80 = 1.81004 \times 10^6, \tag{3.33}$$

which is far too high compared with the real σ_f in the electrolyte (80 S/m). As a result of that, the model predicts too strong electric current through the face f.

Thus, the harmonic interpolation is introduced in our simulation in an attempt of achieving more accurate approximation. The conductivities at the face is:

$$\sigma_f = [\frac{(\delta_N/\delta)}{\sigma_N} + \frac{(\delta_P/\delta)}{\sigma_P}]^{-1} = [\frac{(1/2)}{3.62 \times 10^6} + \frac{(1/2)}{80}]^{-1} = 160 \left(\frac{S}{m}\right), \tag{3.34}$$

which provides a more reasonable estimate of the electrical current at the interface between electrolyte and electrode (14).

Also, in consistency with the harmonic interpolation for σ, the electric potential at the face is implemented using the weighted interpolation with the interpolation weight ϖ. The electric potential at the face is:

$$\phi_f = \varpi \cdot \phi_P + (1 - \varpi)\phi_N, \tag{3.35}$$

where the interpolation weight ϖ reads

$$\varpi = \frac{\delta_N \cdot \sigma_P}{\delta_P \cdot \sigma_N + \delta_N \cdot \sigma_P}. \tag{3.36}$$

3.6 Numerical treatment of equation system; PISO algorithm

All numerical computations are performed using the PISO algorithm to decouple the velocity and pressure in the momentum and continuity equations (5). The advanced algorithm for the marker equation that achieves strong coupling between the classical VOF and multiphase model (2).

The equations are discretized following the finite volume method illustrated in the previous sections. Time derivative terms are discretized using an implicit Euler scheme.

Each time step is solved as a sequence of the following substeps:

1. Solve the marker equation (3.15). Use the velocity and maker fields obtained at the previous time level t^n to update the maker fields α_i of the three layers. Then, update the flow properties fields based on the distribution of the liquid volume fraction.

2. Find the velocity predictor field by solving the discretized momentum equation (3.23) in an implicit manner. Because the exact pressure gradient is not know at this stage the pressure field from last time step p^{n-1} is used. The calculated velocity gives an approximation of new velocity field.

3. Using the calculated velocity predictor field, the operator **H(U)** in equation (3.24) can be assembled and the discretized pressure equation (3.26) can be formulated. Solve the pressure equation (3.26) to get the first estimate of the new pressure field.

4. Update the corrected velocity field with the new pressure field in an explicit manner using equation (3.25).

5. Iterate the step 2 to 4 until the pre-determined tolerance is reached.

6. Solve the electric potential equation (3.31) with the updated velocity implicitly. The harmonic interpolation is used in calculating the electric conductivities to ensure the reasonable electric conductivities at the interface.

7. Update the electric current field with formal FOV manner and the Lorentz force consequently.

CHAPTER IV

Results

The model is designed to study the metal pad instability using the open-source software OpenFOAM. The results include the time evolutions of the velocity, electric current, pressure and electric potential fields as welll as the shapes of the interfaces between the metals and electrolyte. Operational parameters and model setting are described in section 4.1. In section 4.2, the grid sensitivity study is conducted to ensure the reliability of the simulations. A reference case of the metal pad instability is presented in section 4.3. The deformation of the interface between the top layer and electrolyte is observed. The non-dimensional electromagnetic parameter used to describe the metal pad instabilities is introduced in section 4.4. In section 4.5, a parametric study to investigate the relationship between instability and magnitude of magnetic field is presented. In section 4.5.1, the effect of the term $\mathbf{U} \times \mathbf{B}$ in the expression for the Ohm's law $\mathbf{J} = \sigma \cdot (\nabla \phi + \mathbf{U} \times \mathbf{B})$ is investigated. The effect of the electrolyte's thickness is investigated and presented in section 4.6. Finally, the effect of the ratio between the density jumps across the two interfaces is presented in section 4.7.

4.1 Model description

4.1.1 General settings of the model

The interior of a battery is modeled as a cube with side length of 0.1 m. In the reference case, which is considered everywhere except section 4.6, the thickness of the electrolyte

equals to 0.005 m. It is sandwiched between the anode and cathode with thicknesses of 0.0475 m (See Figure 4.1).

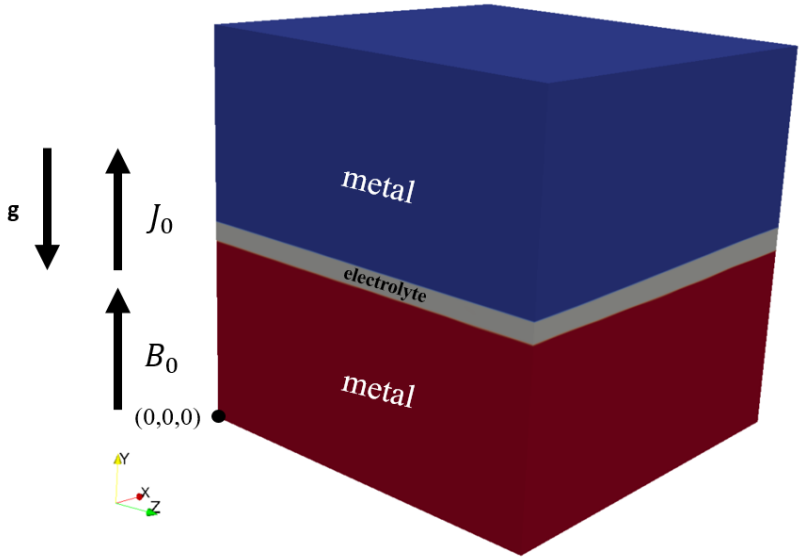

Figure 4.1: The geometry of the model with coordinate system.

Because of the immiscibility of the three liquids, distinct physical properties are assigned to each layers. The properties are given in table 4.1.

	h	ρ	υ	σ
unit	cm	kg/m^3	m$^2/s$	S/m
Negative electrode(top)	4.75	1577	6.70×10^{-7}	$3.62 \times 10^{+6}$
Electrolyte(middle)	0.5	1715	6.80×10^{-7}	80
Positive electrode(bottom)	4.75	6270	1.96×10^{-7}	$8.66 \times 10^{+5}$

Table 4.1: Physical parameters of the reference case. Physical properties of liquids in different layers. Unperturbed layer thickness h, density ρ, kinematic viscosity υ and electric conductivities σ are shown.

4.1.2 Initial conditions

4.1.2.1 Marker field α

The marker field α determines the distribution of the electrolyte and the two metals. Initially, the distribution is that of three horizontal layers with a small perturbation of the

interface between the top and middle layers. The bottom-electrolyte interface remains flat. The perturbation of the top interface is set as an inclined plane with small slope k (=1/50). The maximum perturbation amplitude is: $\varepsilon = k \times 0.1m = 0.1 * (1/50) = 2(mm)$.

4.1.2.2 Electrical potential field ϕ

The initial condition is defined in equivalence with the unperturbed vertical electric current $\mathbf{J} = 7850\, A/m^2$. From the electrical potential equation ($\mathbf{J} = -\sigma\nabla\cdot\phi$) in the absence of flow, the initial distribution of the electrical potential ϕ can be expressed as solution of the equation:

$$\sigma \cdot (\frac{\partial\phi}{\partial x}, \frac{\partial\phi}{\partial y}, \frac{\partial\phi}{\partial z}) = (0, -7850, 0), \tag{4.1}$$

where σ is different for different layers.

The initial distributions of electrical potential ϕ and marker α can be initialized by the OpenFOAM's field-setting function 'funkySetFields' based on the expressions above.

4.1.3 Boundary conditions

4.1.3.1 Boundary conditions for ϕ

For the boundary conditions for ϕ, zero-gradient is applied at the side walls of cell.

The boundary conditions for the top and bottom walls are defined according to the equation (4.1). Integrating (4.1) rewritten as:

$$\sigma_i \cdot \frac{\mathrm{d}\phi}{\mathrm{d}y} = -7850\ \frac{A}{m^2}, \tag{4.2}$$

where σ_i represents the electrical conductivities in different layers, we obtain

$$\Delta\phi = \phi_{top} - \phi_{bottom} = -0.4912\ V. \tag{4.3}$$

The condition is assumed to remain valid when the interfaces are perturbed.

Hence, the boundary conditions at the top and bottom are specified as

$$\phi_{top} = -4.912 \times 10^{-01}\ V \quad and \quad \phi_{bottom} = 0\ V.$$

4.2 Grid sensitivity tests

In order to achieve accurate results with good computational efficiency, the grid sensitivity tests are conducted. We expect stronger gradients of velocity and other fields in the vertical than in the horizontal directions. Therefore, denser meshes should be applied along the vertical direction. Furthermore, dense mesh particularly in the vertical direction is needed in the areas of two interfaces, so that the interface deformation and the resulting changes in the electric currents are reproduced correctly. To save the computational resources, the grading (nonuniform) mesh is implemented. Small vertical grid steps Δy_{min} are used in and around the interfaces. Outside this area, Δy is increased in a manner of geometric progression to $\Delta y_{max} = 10^{-3}$ at the top/bottom of the model. The resulting mesh is illustrated in Figure.4.4.

In the grid sensitivity test, the parametric study is conducted by changing the unit length of the cell Δy_{min} as well as Δx and Δz. The grid is deemed sufficient if further refinement does not bring significant change in the time period and the peak value of the curve of the velocity time signal at a given point. The test parameters are shown in table 4.2.

Δx	Δy_{min}	Δz	Δt	Time period	Execution Time
m	m	m	s	s	s
2×10^{-3}	1×10^{-4}	2×10^{-3}	1×10^{-3}	3.34	245158
2×10^{-3}	2×10^{-4}	2×10^{-3}	1×10^{-3}	3.32	81533.2
2×10^{-3}	5×10^{-4}	2×10^{-3}	1×10^{-3}	3.34	39379.1
1×10^{-3}	2×10^{-4}	1×10^{-3}	1×10^{-3}	3.29	242300
2×10^{-3}	2×10^{-4}	2×10^{-3}	5×10^{-4}	3.33	144624
2×10^{-3}	2×10^{-4}	2×10^{-3}	2×10^{-3}	3.26	40321.6
2×10^{-3}	2×10^{-4}	2×10^{-3}	4×10^{-3}	3.27	22570.6
2×10^{-3}	2×10^{-4}	2×10^{-3}	5×10^{-3}	3.29	20063.4

Table 4.2: Grid sensitivity study for $\mathbf{B} = (0,10,0)\ mT$ and $\mathbf{J_0} = (0,7850,0)\ A/m^2$. The model is simulated with side length of 0.1 m, thickness of electrolyte 0.005 m with small initial perturbation(see text). The properties of the metals and electrolyte are in Table 4.1. For each case, the 10 seconds of the cell's evolution are simulated. Execution time of the run on 8 CPUs of our cluster is also shown.

4.2.1 Effect of Δy_{min}

The results are presented in Table 4.2 and Figure 4.2. We see that the grid step affects the time period of the fluctuations very little. The simulations with $\Delta y_{min} = 5\times10^{-4}m$ predict clearly incorrect values of the vertical current (see Figure 4.2). We attribute this to poor resolution of the interface zone, which leads to underestimating the local electrical resistance. There is no significant difference between the velocity and current curves at $\Delta y_{min} = 1\times10^{-4}\ m$ and $\Delta y_{min} = 2\times10^{-4}\ m$ while it take much more computational time to simulate with the $\Delta y_{min} = 1\times10^{-4}\ m$. Therefore, we take $\Delta y_{min} = 2\times10^{-4}\ m$ as the optimal grid size, at which a compromise between the computational accuracy and computational time is achieved.

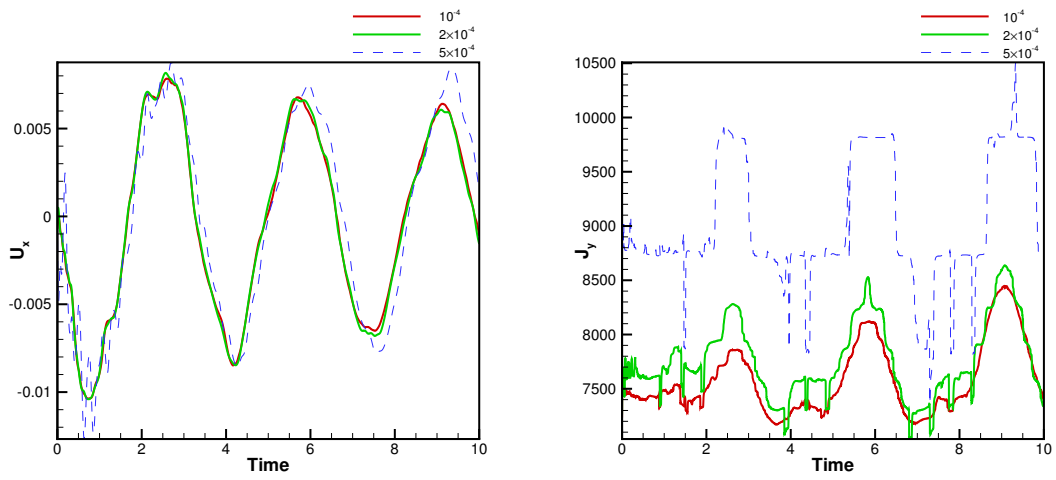

Figure 4.2: The signals of horizontal velocity U_x at the point x=0.05 m, y=0.049 m, z=0.016 m (within the electrolyte) is shown on the left. The signals of vertical current J_y at the point x=0.05 m, y=0.06 m, z=0.016 m (within the top layer) is shown on the right.

4.2.2 Effect of $\Delta x = \Delta z$

The computed results are less sensitive to the horizontal grid size. We see that the horizontal grid step affects the time period of the fluctuations very little. The simulations with $\Delta x = \Delta z = 2 \times 10^{-3}$ and $\Delta x = \Delta z = 1 \times 10^{-3}$ predicts identical value for the curve of horizontal velocity U_x and vertical current J_y (see Figure 4.3). We conclude that the computed results are less sensitive to the horizontal than to vertical grid size. Therefore, the $\Delta x = \Delta z = 2 \times 10^{-3}$ is used in the simulations.

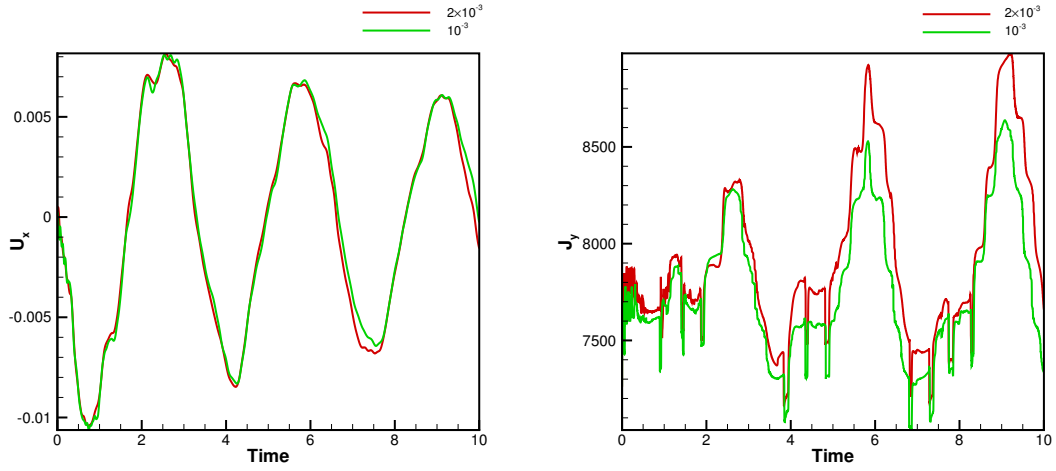

Figure 4.3: The signals of horizontal velocity U_x at the point x=0.05 m, y=0.049 m, z=0.016 m (within the electrolyte) is shown on the left. The signals of vertical current J_y at the point x=0.05 m, y=0.06 m, z=0.016 m (within the top layer) is shown on the right.

The final mesh with $x \times y \times z = 50 \times 170 \times 50$ cells used in the simulations is illustrated in Figure 4.4.

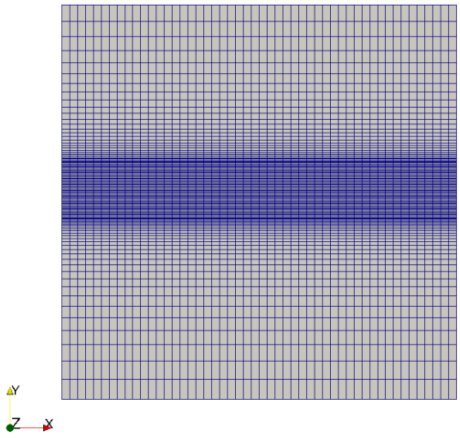

Figure 4.4: The mesh determined as optimal in the grid sensitivity testing.

4.2.3 Effect of Δt

The results of the time step sensitivity test are presented in this section. The optimal mesh shown in Figure 4.4 is used. The numerical stability of the code requires that the

Courant number $Co = \Delta t \left(\frac{U_x}{\Delta x} + \frac{U_y}{\Delta y} + \frac{U_z}{\Delta z} \right)$ is kept below 0.5. With the optimal mesh described above, the Δt should be smaller than 5×10^{-3} s.

Considering that the first order scheme is used for time discretization, Δt much smaller than the numerical stability limit may be needed for numerical accuracy.

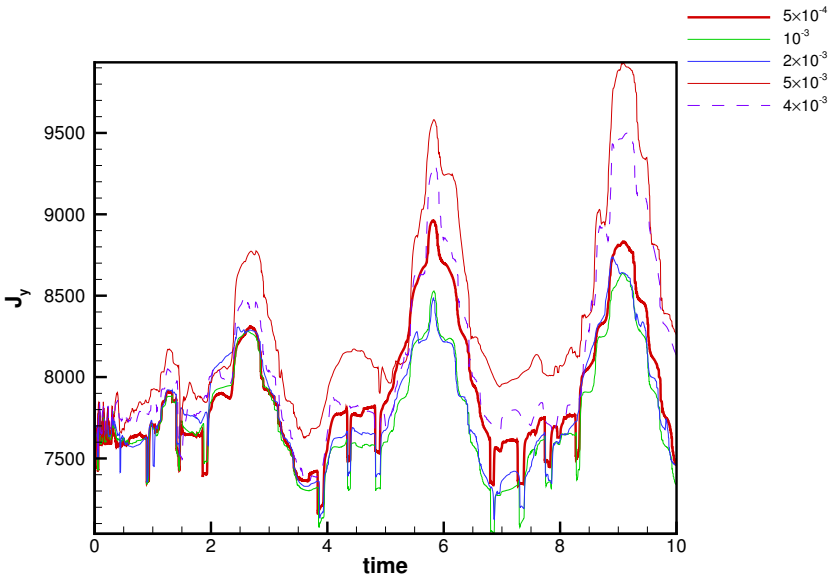

Figure 4.5: The signals of vertical electric current J_y at point x=0.05 m, y=0.049 m, z=0.016 m (within the electrolyte) for various values of the time step Δt.

The parametric study of the effect of Δt ranged between 5×10^{-4} s to 5×10^{-3} is conducted. The basic purpose is to find the Δt optimizing the relation between the computational time and accuracy. The results illustrated in Figure 4.5 and 4.6 indicate that there is no significant difference for the velocity U_x curve while serious differences exist among the curves for electric curves. The reason for this remains unclear. We leave this question to further studies and use. $\Delta t = 4 \times 10^{-3}$ s as the best option that can produce reasonably accurate results in relatively short time.

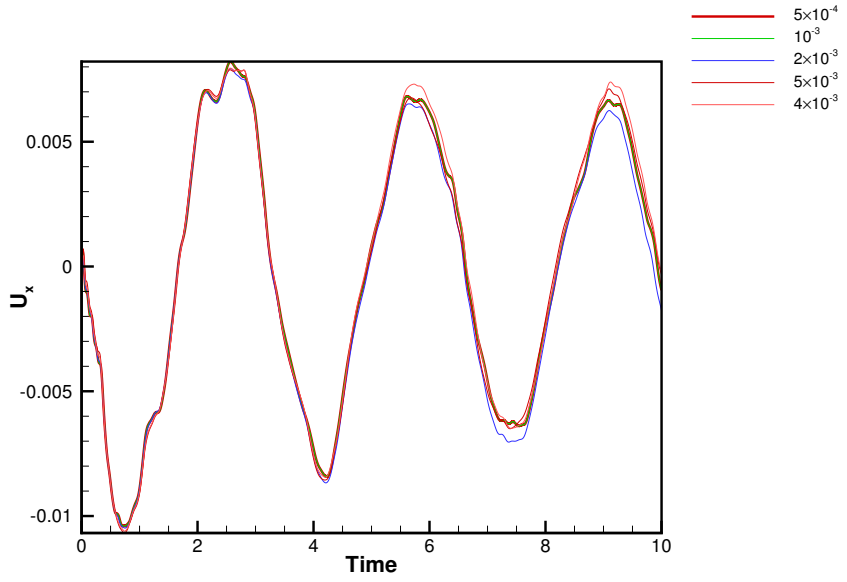

Figure 4.6: The signals of horizontal velocity U_x at point x=0.05 m, y=0.049 m, z=0.016 m (within the electrolyte) for various values of the time step Δt.

Note that this value of the time step Δt might become invalid in the case of larger magnetic field. A stronger magnetic field leads to stronger instability and, thus, higher flow velocity. Smaller time steps are, therefore, needed to satisfy the Courant-Friedrichs-Lewy(CFL) condition (26).

4.3 Reference case

A reference case for the metal pad instability at $B_y = 10mT$, $J_y = 7850\ A/m^2$ and $h_{electrolyte} = 5mm$ is presented in this section. The properties of the liquid metal and electrolyte are listed in Table.4.1.

We find that the metal pad instability is predicted by the solver. With the magnetic field $\mathbf{B_y} = 10mT$, the system is evidently unstable. After a short period of growing, the small initial perturbation gives rise to periodic oscillations at the interface between the top metal and the electrolyte.

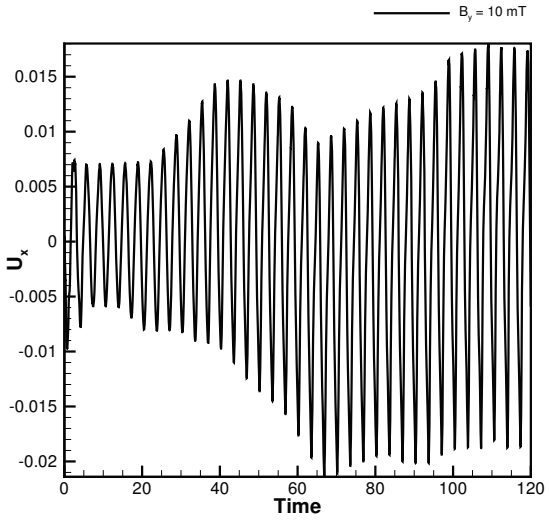

Figure 4.7: The signal of U_x at the $B_y = 10mT$ is presented as a reference case. The probe point is inside the electrolyte during the entire simulation. The metal pad instability results in growing a periodic oscillations, which represent growing sloshing waves at the interface.

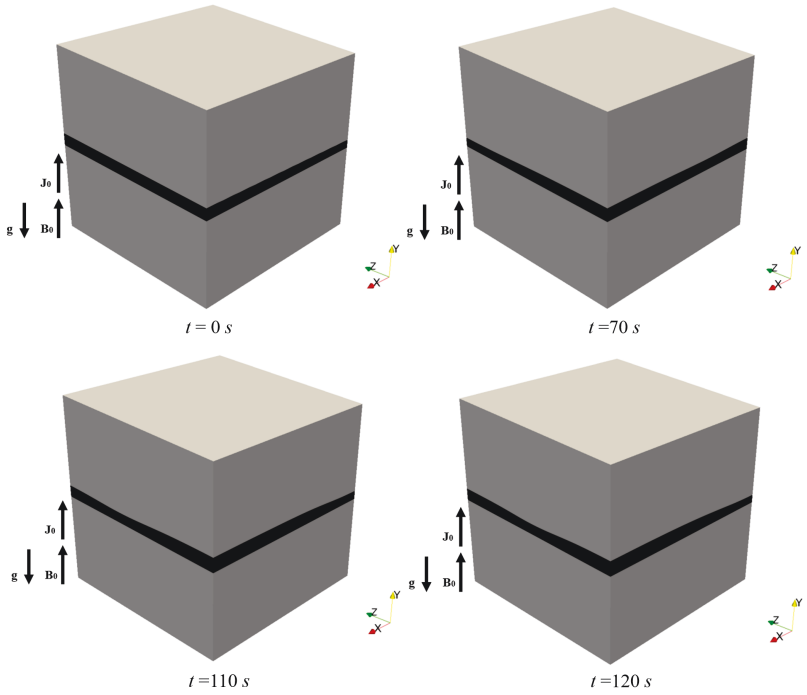

Figure 4.8: Evolution of the metal pad instability at different time $t = 0s$, $t = 70s$, $t = 110s$, $t = 120s$.

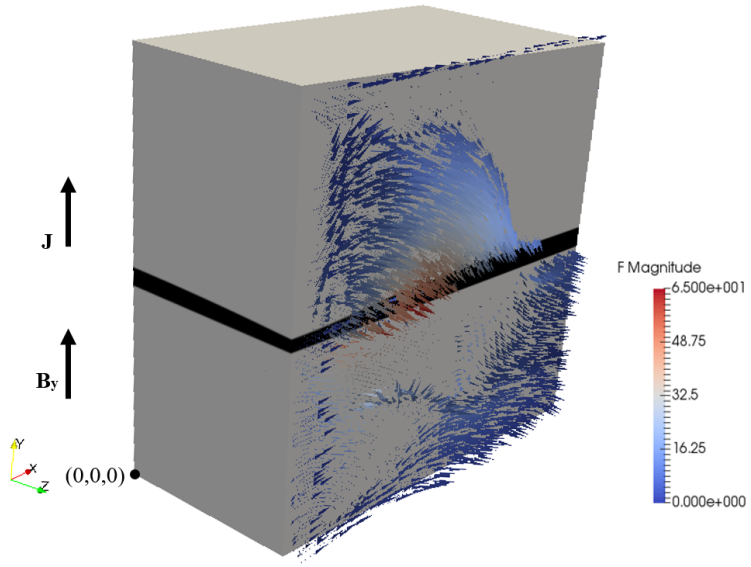

Figure 4.9: Vectors of Lorentz force in the cross-section $z = 0.05m$ for the reference case flow at $t = 120s$.

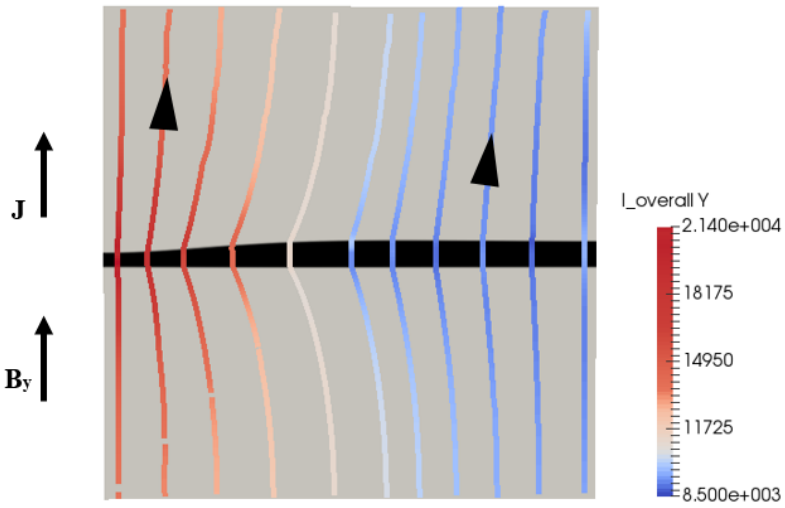

Figure 4.10: Streamlines of electric currents in the cross-section $z = 0.05m$ for the reference case flow at $t = 120s$.

4.4 Instability parameters

It has been suggested in the recent works ((22), (28)) that in the case when the instability occurs at only one interface, it is largely controlled by the non-dimensional electromagnetic parameter similar to that found earlier for the aluminum reduction cells. For example, for the upper interface at $\Delta\rho^A \ll \Delta\rho^B$, the parameter is:

$$\Pi \equiv \frac{J_0 B_0 L_x L_z}{\Delta\rho^A h_0^E h_0^A g}, \tag{4.4}$$

where J_0, B_0, L_x, L_z, $\Delta\rho^A = \rho^{electrolyte} - \rho^{top\ layer}$, h_0^E, h_0^A and g are the base electric current, vertical component of the magnetic field, side length of cubic in x-axis direction, side length of cubic in z-axis direction, the density difference between top layer and electrolyte, unperturbed thickness of electrolyte, unperturbed thickness of top layer and acceleration of gravity respectively.

An analogous parameter exists for the instability developing at the lower interface at $\Delta\rho^A \gg \Delta\rho^B = \rho^{bottom\ layer} - \rho^{electrolyte}$:

$$\Pi \equiv \frac{J_0 B_0 L_x L_z}{\Delta\rho^B h_0^E h_0^B g}. \tag{4.5}$$

According to previous studies in (28), the interface instability will be more complicated if $\Delta\rho^A \sim \Delta\rho^B$. The interface deformation is taking effect on both top and bottom interface, which might give rise to coupling effect.

The validity of these criteria is partially tested in the following sections.

4.5 Effect of the strength of magnetic field

The parametric study of the effect of the strength of the magnetic field is presented in this section. We change the magnitude of B_y while keeping the other parameters of the system unchanged. It is expected that the destabilization effect will increase at higher B_y.

The growth rate of the perturbations is not considered as a measurement for the instability. We have found that OpenFOAM is not a good tool for computing evolution of infinite small perturbations due to the slowness of calculations and the inaccuracy in reproduction of small amplitude motions of the interface. All the simulations are conducted for weak but finite-amplitude perturbations, i.e. in the nonlinear regime. Furthermore, in reality, the instability of interface in the liquid metal batteries is already strong invoked by other mechanisms such as thermal convection(18).

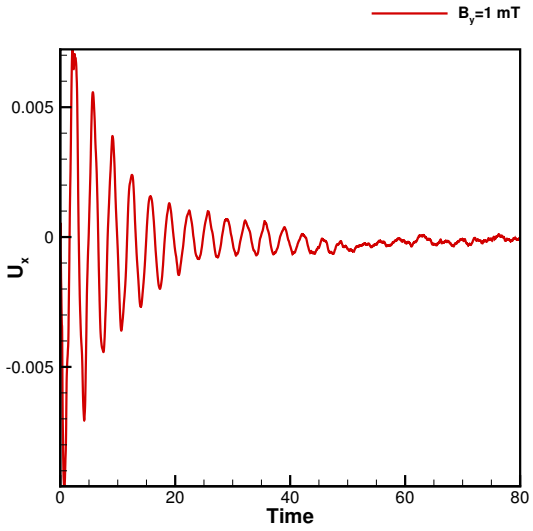

Figure 4.11: Signal of U_x at $B_y = 1\ mT$. There is no metal pad instability at this magnetic field. The initial perturbation is neutralized by gravity and the flow become zero eventually.

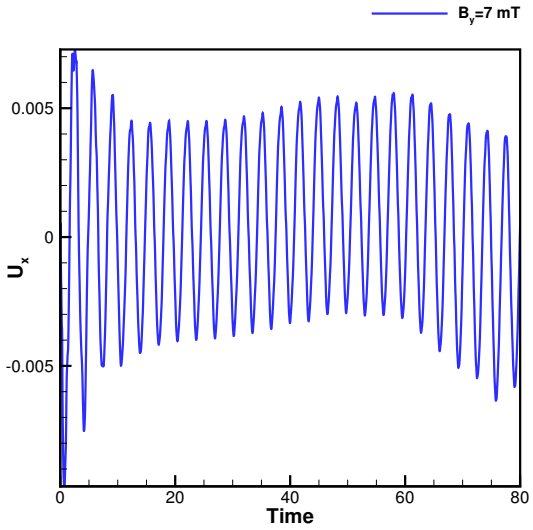

Figure 4.12: Signal of U_x at $B_y = 7\ mT$. There is no metal pad instability at this magnetic field. The metal pad instability grows into periodic oscillations without decaying.

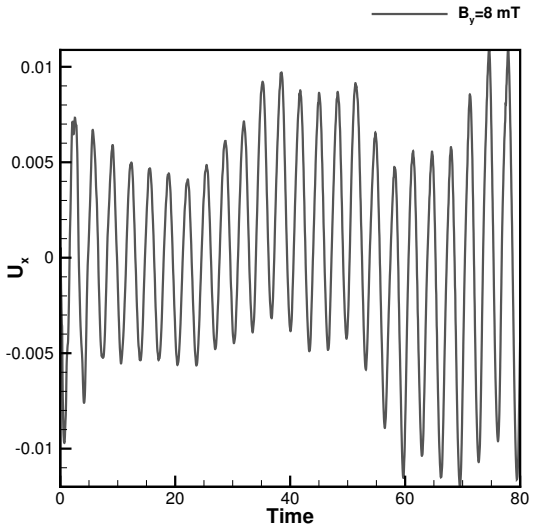

Figure 4.13: Signal of U_x at $B_y = 8\ mT$. The metal pad instability grows very slowly. The system may be in a state close to the threshold of the metal pad instability.

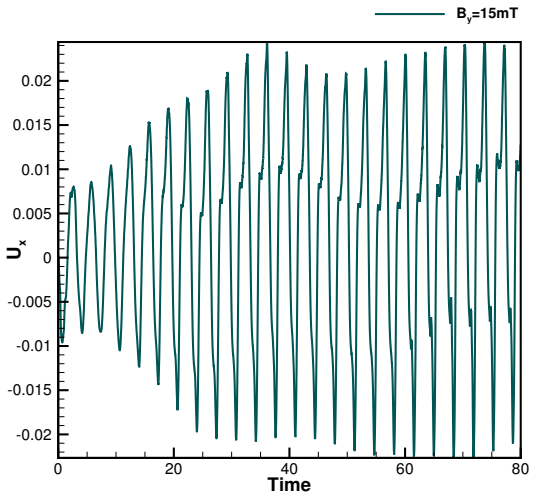

Figure 4.14: Signal of U_x at $B_y = 15\ mT$. The amplitude of the oscillations keeps growing with active interface deformation until it saturates at a high amplitude. We consider this flow as strongly unstable.

The results about the magnetic fields comparison illustrate the fact that the battery becomes more unstable with the increase of the magnetic fields.

4.5.1 Effect of $\sigma \mathbf{U} \times \mathbf{B}$ in the Ohm's law

Recalling the Ohm's law for a moving conductor:

$$\mathbf{J} = \sigma \left(\nabla \phi + \mathbf{U} \times \mathbf{B} \right). \tag{4.6}$$

Two simulations are conducted. One uses the full expression (4.6). In the other case, the $\sigma \mathbf{U} \times \mathbf{B}$ term is removed from (4.6) and, respectively, from the electric potential equation (2.6).

It has been suggested in simpler (for example linearized or shwllow water) models of the instability that the effect of the magnetic force is insignificant and the simulations can be simplified by neglecting the effect of $\sigma \mathbf{U} \times \mathbf{B}$ (28).

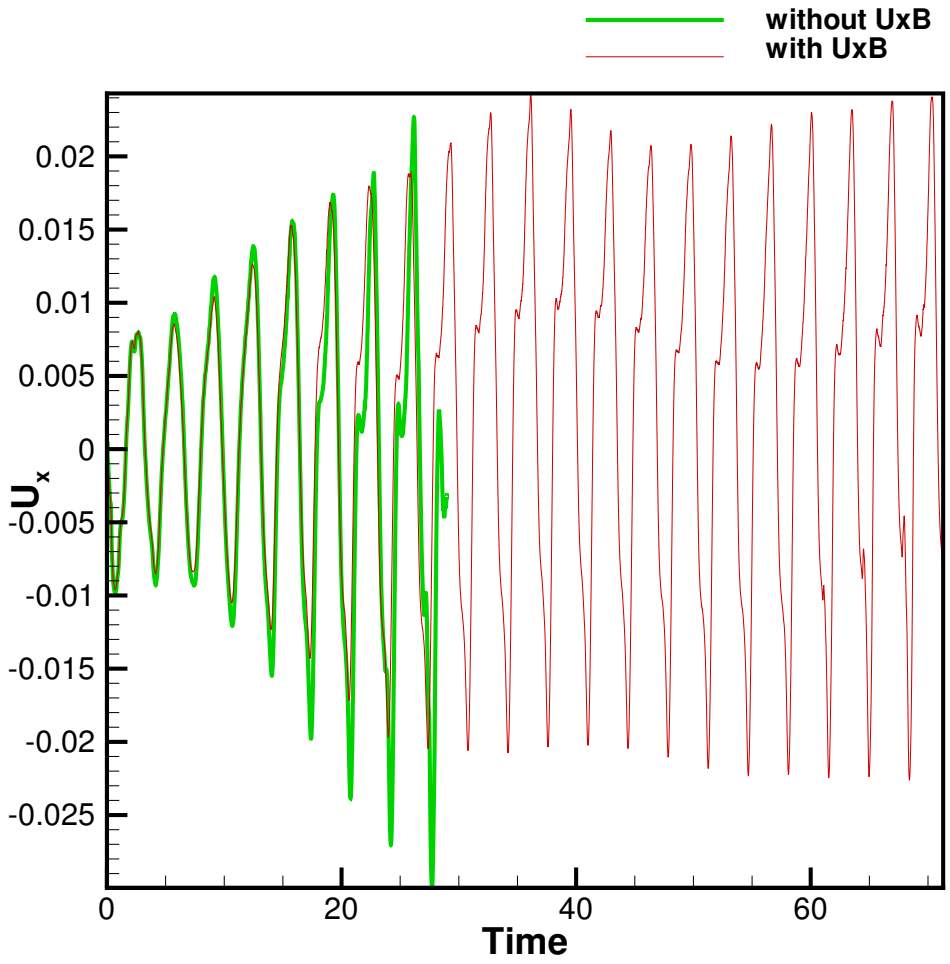

Figure 4.15: The effect of the second term of Lorentz force is investigated. The simulations are conducted under the $B_y = 15\ mT$. The simulation with $\sigma \mathbf{U} \times \mathbf{B}$ show periodic oscillations in the saturated stage after the growth of instability, while the simulation without $\sigma \mathbf{U} \times \mathbf{B}$ does not allow saturation and results in further growth and short circuit between the metal layers.

However, the comparison between the results of the two runs shows that the second term in Ohm's law $\sigma \mathbf{U} \times \mathbf{B}$ has an effect as a stabilized term and cannot be neglected as presented in Figure 4.15.

4.6 Effect of thickness of electrolyte

The effect of the thickness of the electrolyte is discussed in this section. In order to analyze this effect, the following thicknesses shown in Table 4.3 are simulated in our study.

$h_{electrolyte}$	Time period τ	Π
mm	s	
3	4.35	5.984
5	3.43	3.666
7	3.04	2.675
10	2.69	1.935

Table 4.3: Effect of electrolyte thickness for $\mathbf{B} = (0, 15, 0)\ mT$ and $\mathbf{J_0} = (0, 7850, 0)\ A/m^2$ with side length of 0.1 m. The properties of the metals and electrolyte are in Table 4.1. Each case is executed for 80 seconds, changing $h_{electrolyte}$ while keeping the other settings unchanged.

It is predicted in the earlier studies and suggested by the non-dimensional criterion (4.4) that the thickness of the electrolyte is one of the key factors for the metal pad instability ((22), (28)).

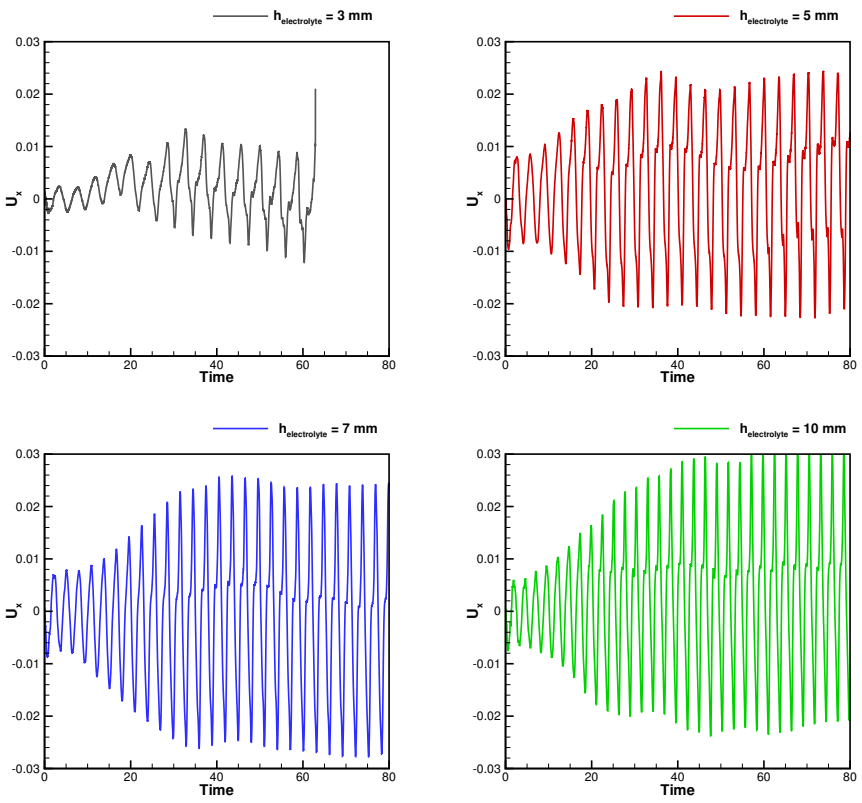

Figure 4.16: Time signals of the horizontal velocity U_x at the point x=0.05 m, y=0.049 m, z=0.016 m (within the electrolyte) for the cases with various $h_{electrolyte}$ presented in Table 4.3.

We find that the thinner the electrolyte, the more unstable the system is. The time period of instability oscillation decreases with increasing of $h_{electrolyte}$ as shown in Figure 4.16.

4.7 Effect of density ratio

The effect of the density jumps across the interfaces is analyzed in this section. A parametric study is conducted, in which we keep constant $\rho^{top\ layer}$ and $\rho^{bottom\ layer}$, but vary $\rho^{electrolyte}$. The following densities of the electrolyte $\rho^{electrolyte}$ shown in Table 4.4 are simulated in our study.

$\rho^{electrolyte}$	Time period τ	Π
kg/m^3	s	
1646	4.64	7.332
1715	3.43	3.666
2083	2.02	1
5994	0.48	1.833
6132	0.48	3.666

Table 4.4: Effect of the density jumps for $\mathbf{B} = (0, 15, 0)\ mT$, $h_{electrolyte} = 5\ mm$ and $\mathbf{J_0} = (0, 7850, 0)\ A/m^2$ with side length of 0.1 m. The properties of the metals and electrolyte are in Table 4.1. Each case is executed by changing $\rho^{electrolyte}$ while keeping the other settings unchanged.

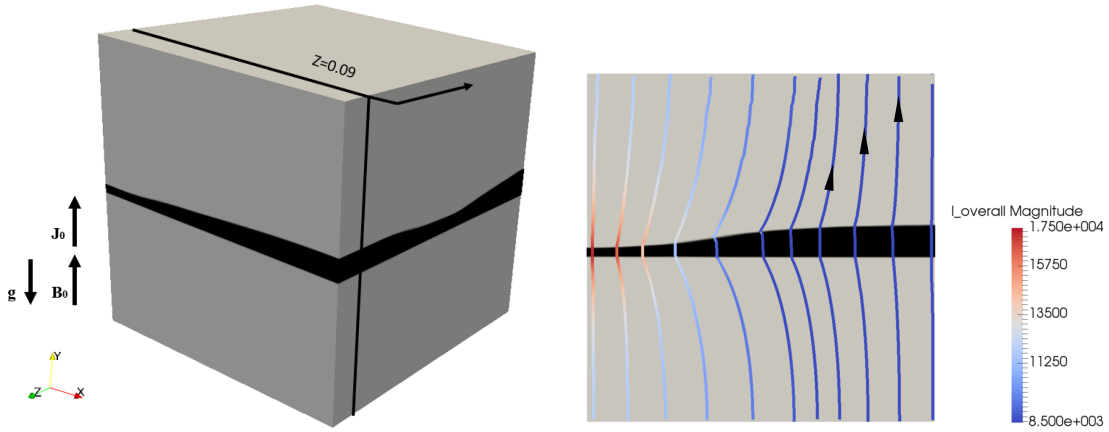

Figure 4.17: Metal pad instability and streamlines of electric currents in the cross-section $z = 0.09m$ for $\Pi = 7.332$ at $t = 13s$.

Given that $\Delta\rho^A \ll \Delta\rho^B$, we find that the significant deformations are expected at the upper interface at $\Pi = 7.332$ (See Figure 4.17). Frequencies and magnitudes of instability oscillation increase with increasing of Π(See Figure 4.18).

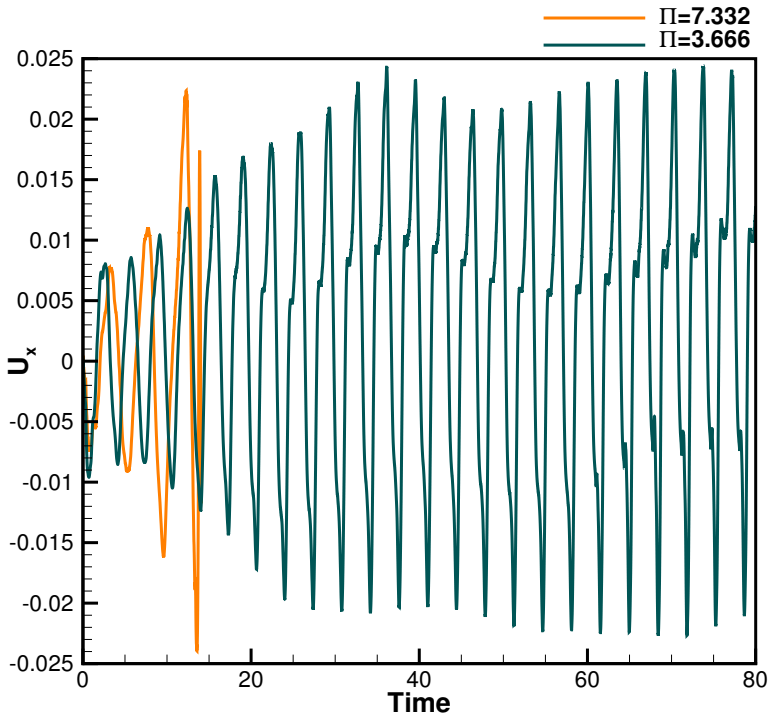

Figure 4.18: Time signals of the horizontal velocity U_x at the point x=0.05 m, y=0.049 m, z=0.016 m (within the electrolyte) for the cases with various $\rho^{electrolyte}$ presented in Table 4.4.

We have also performed simulations with $\Delta\rho^A \gg \Delta\rho^B$ and expect two dominating frequencies in the Figure 4.19 and Figure 4.20. It is predicted in the earlier studies (12) that the flow dynamics is complex due to the coupling effect of the two metal-electrolyte interfaces. We will leave it for future studies.

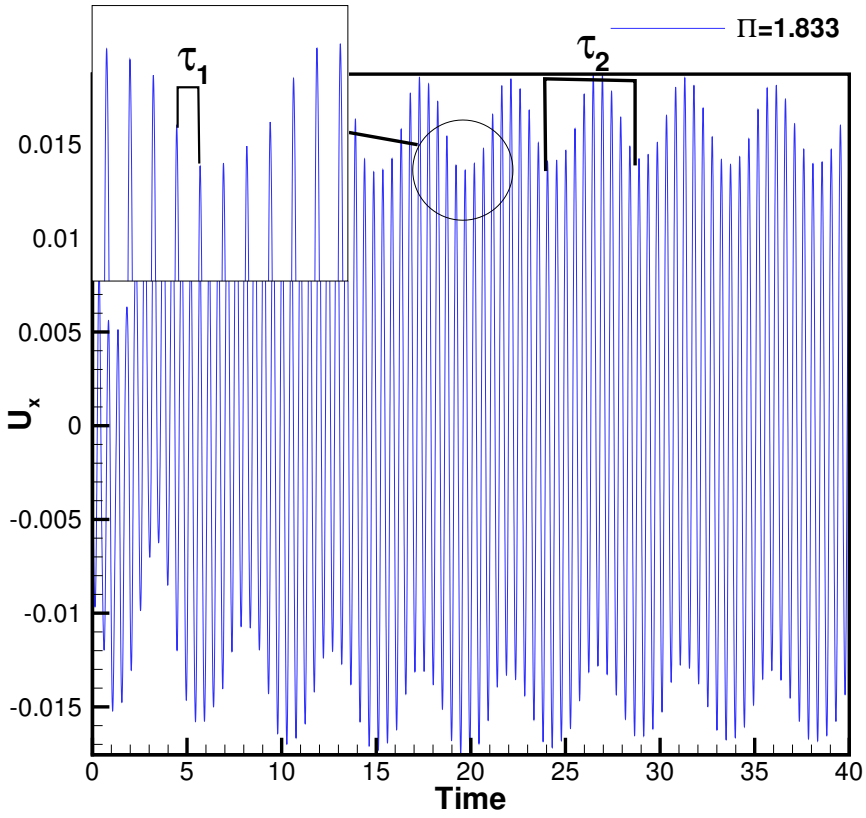

Figure 4.19: Time signals of the horizontal velocity U_x at the point x=0.05 m, y=0.049 m, z=0.016 m (within the electrolyte) for the case with $\Pi = 1.833$ presented in Table 4.4. Two main time periods are observed with $\tau_1 = 0.48\ s$ and $\tau_2 = 5.08\ s$

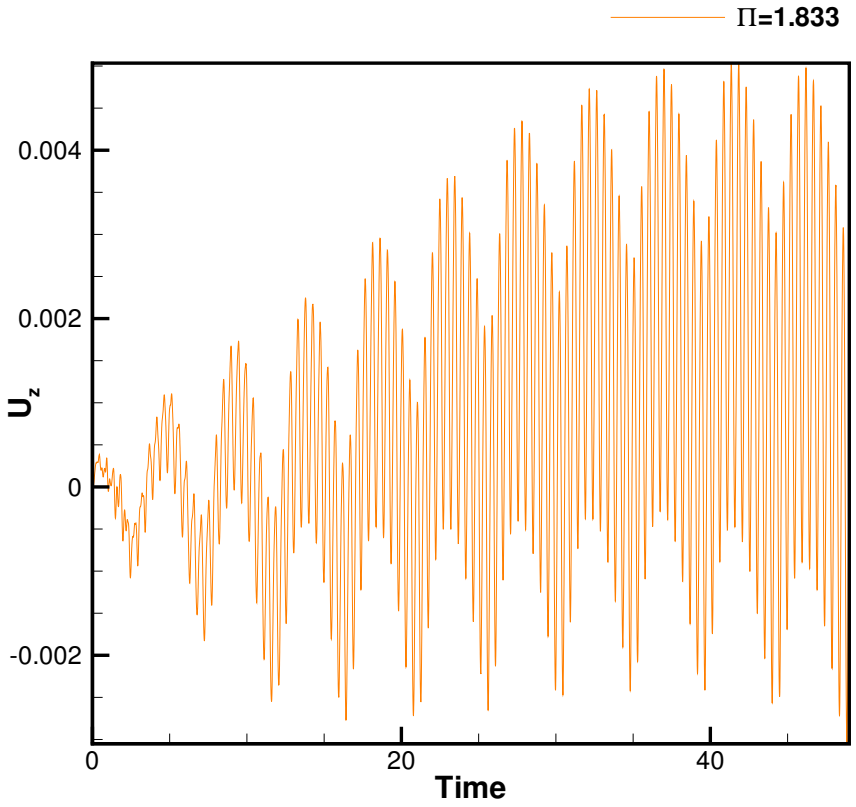

Figure 4.20: Time signals of the horizontal velocity U_z at the point x=0.05 m, y=0.049 m, z=0.016 m (within the electrolyte) for the case with $\Pi = 1.833$ presented in Table 4.4.

CHAPTER V

Conclusions

We have studied the metal pad instability in the Liquid Metal Batteries(LMBs) with vertical magnetic field $\mathbf{B_0}$. The main conclusion is that, *the magnetic field induced by neighboring cells and supply lines can potentially affect the operation of LMBs and should always be considered in the design of the devices*. We find that the the metal pad instabilities can be simulated by the open-source CFD software OpenFOAM. The effect of the metal pad instability can be controlled by the magnetic field B_0, the vertical electric current J_0, the geometry parameters of the LMBs such as the thickness of the electrolyte $h_{electrolyte}$ and the density jumps across the interfaces $\Delta\rho^A$ *or* $\Delta\rho^B$.

Our results indicate that the effect of the metal pad instability has positive correlation with the magnitude of B_0 and J_0 while has negative correlation with the thickness of electrolyte $h_{electrolyte}$ and the density jumps of the interfaces $\Delta\rho^A$ *or* $\Delta\rho^B$. The accuracy of the simulations is limited by the numerical error from the solution of multiphase flow problem. The numerical error is enlarged by substantial difference in electrical conductivities among metal/electrolyte layer. We leave this interesting problem for future studies.

BIBLIOGRAPHY

[1] **A. Prosperetti, G. T.** 2007. *Computational methods for multiphase flow*. Cambridge University Press.

[2] **Berberović, E., N. P. van Hinsberg, S. Jakirlić, I. V. Roisman, and C. Tropea.** 2009. Phys. Rev. E **79**:036306.

[3] **Davidson, P. A.** 2001. *An Introduction to Magnetohydrodynamics*. Cambridge Texts in Applied Mathematics. Cambridge University Press.

[4] **Dunn, B., H. Kamath, and J.-M. Tarascon.** 2011. Science **334** (6058):928–935.

[5] **Issa, R. I.** 1986. Journal of Computational Physics **62** (1):40 – 65.

[6] **Jasak, H., and A. Jemcov.** 2007. p. 1–20. *In:* International Workshop on Coupled Methods in Numerical Dynamics, IUC .

[7] **Kabir, M. M., and D. E. Demirocak.** a. . International Journal of Energy Research **41** (14):1963–1986.

[8] **Kelley, D. H., and T. Weier.** 2018. Applied Mechanics Reviews .

[9] **Kim, H., D. A. Boysen, J. M. Newhouse, B. L. Spatocco, B. Chung, P. J. Burke, D. J. Bradwell, K. Jiang, A. A. Tomaszowska, K. Wang, W. Wei, L. A. Ortiz, S. A. Barriga, S. M. Poizeau, and D. R. Sadoway.** 2013. Chemical Reviews **113** (3):2075–2099.

[10] **Knaepen, B., S. Kassinos, and D. Carati.** 2004. Journal of Fluid Mechanics **513**:199220.

[11] **Köllner, T., K. Schwarzenberger, K. Eckert, and T. Boeck.** 2013. Physics of Fluids **25** (9):092109.

[12] **Maik Horstmann, G., N. Weber, and T. Weier.** 2017. ArXiv e-prints .

[13] **Moukalled, F., L. Mangani, and M. Darwish.** 2015. *The Finite Volume Method in Computational Fluid Dynamics: An Advanced Introduction with OpenFOAM® and Matlab*. Fluid Mechanics and Its Applications. Springer International Publishing.

[14] **Patankar, S. V.** 1980. *Numerical heat transfer and fluid flow*. Series on Computational Methods in Mechanics and Thermal Science. Hemisphere Publishing Corporation (CRC Press, Taylor & Francis Group).

[15] **Rusche, H.** 2002. *Computational Fluid Dynamics of Dispersed Two-phase Flows at High Phase Fractions*. PhD thesis Imperial College of Science, Technology and Medicine.

[16] **Seilmayer, M., F. Stefani, T. Gundrum, T. Weier, G. Gerbeth, M. Gellert, and G. Rüdiger.** 2012. Phys. Rev. Lett. **108**:244501.

[17] **Sele, T.** 1977. Metallurgical Transactions B **8** (4):613–618.

[18] **Shen, Y., and O. Zikanov.** 2016. Theoretical and Computational Fluid Dynamics **30** (4):275–294.

[19] **Sneyd, A. D., and A. Wang.** 1994. Journal of Fluid Mechanics **263**:343360.

[20] **Stefani, F., T. Weier, T. Gundrum, and G. Gerbeth.** 2011. Energy Conversion and Management **52** (8):2982 – 2986.

[21] **Ubbink, O.** 1997. *Numerical prediction of two fluid systems with sharp interfaces*. PhD thesis Imperial College of Science, Technology and Medicine.

[22] **Weber, N., P. Beckstein, W. Herreman, G. M. Horstmann, C. Nore, F. Stefani, and T. Weier.** 2017. Physics of Fluids **29** (5):054101.

[23] **Weber, N., V. Galindo, J. Priede, F. Stefani, and T. Weier.** 2015. Physics of Fluids **27** (1):014103.

[24] **Weber, N., V. Galindo, F. Stefani, and T. Weier.** 2014. Journal of Power Sources **265**:166 – 173.

[25] **Weier, T., A. Bund, W. El-Mofid, G. M. Horstmann, C-C. Lalau, S. Landgraf, M. Nimtz, M. Starace, F. Stefani, and N. Weber.** 2017. title **228** (1):012013.

[26] **Zikanov, O.** 2010. *Essential Computational Fluid Dynamics*. Wiley.

[27] **Zikanov, O.** 2015. Phys. Rev. E **92**:063021.

[28] **Zikanov, O.** 2018. Theoretical and Computational Fluid Dynamics .